A study on droplets dispersion and deposition characteristics under supersonic spray flow for nanomaterial coating applications

Semih Akin [a], Puyuan Wu [a], Jung-Ting Tsai [b], Chandra Nath [a], Jun Chen [a], Martin Byung-Guk Jun [a],[*]

[a] School of Mechanical Engineering, Purdue University, West Lafayette, IN 47907, United States
[b] School of Materials Engineering, Purdue University, West Lafayette, IN 47907, United States

ARTICLE INFO

ABSTRACT

Supersonic spray coating of nanomaterials, owing to high impact velocity of particles, offers significant potential to improve the physical and mechanical properties of target surfaces. Rather than handling individual light nano-scale particles directly with a number of limitations, aqueous nanomaterial colloids and suspensions can be supersonically deposited onto surfaces by converting these complex liquid mixtures into the form of atomized micro-scale droplets. Dispersion and deposition characteristics of these droplets play a vital role in the quality and efficacy of the resultant nanomaterial coating. In the present study, comprising numerical modeling and experimental validation, we investigate details of the dispersion and deposition characteristics of droplets under supersonic flow conditions. In the numerical study, a two-way coupled discrete phase modeling is used to track the discrete phase (*i.e.*, droplets) and to investigate the interaction of droplets with the continuous gas phase (*i.e.*, high-velocity driving gas) in regard to their properties and conditions. The results through computational fluid dynamics (CFD) show that driving gas properties (*i.e.*, temperature, pressure, gas type) and droplet size play a prominent role in droplets dispersion and deposition phenomena. In particular, smaller droplets (≤ 2 μm) are observed to be more susceptible to turbulent dispersion and evaporation. In the experimental study, an atomization-based supersonic spray system is developed for model validation and a case example of nano-coating applications. The CFD modeling results are validated by particle image velocimetry (PIV) measurements. A case study of titanium dioxide (TiO_2) nanomaterial coating on a polymer substrate (ITO/PET film) is performed to demonstrate the suitability of the present spray deposition system, which also addresses the current challenges of TiO_2 coating onto ITO/PET surface.

1. Introduction

Nowadays, nanomaterials attract much attention owing to their unique properties, structural tunability, and a wide range of applications in electronics, automotive, packaging, energy, and so on. Various types of nanomaterials have been increasingly developed and applied in many industries. To deposit the nanomaterials on solid surfaces for coating applications, a variety of spray or printing techniques are explored. However, it remains a major challenge in the nanocoating technology to develop efficient nanomaterial delivery systems in order to impinge or deposit nanomaterials onto target surfaces so that end-users can effectively utilize their inherent properties.

Many coating technologies, such as chemical vapor deposition (CVD), physical vapor deposition (PVD), spin coating, pulsed laser deposition (PLD), inkjet printing, aerosol jet printing (AJP), and cold spray deposition have been currently used [1–6]. Despite great promises, most of these methods have significant limitations in nanomaterial coating. In recent years, cold spray deposition method (*i.e.*, also called cold gas spray, cold gas dynamic spray, kinetic spray) has attracted widespread interest in the solid-state supersonic deposition of various materials onto surfaces without a need for high temperature and vacuum [6,7]. Although conventional cold spraying has been widely used for deposition of solid-state microscale particles in a size range of 5–50 μm, previous studies have reported that individual nanoparticles (*i.e.*, <0.1 μm) cannot be cold sprayed due to their insufficient inertia and momentum to penetrate the inherent bow shock zone that is formed near the substrate [8–10].

As schematically shown in Fig. 1a, the trajectory of the individual nanoparticles is significantly affected by the bow shock region, and they

Nomenclature

A	Area
C_c	Cunningham slip correction factor
C_s	vapor concentration at the droplet surface
C_∞	vapor concentration of the bulk flow
D_m	Diffusion coefficient for species
e	Specific internal energy
$\vec{F}$	Force vector
$\overrightarrow{F_{Ba}}$	Basset force
$\overrightarrow{F_{Bu}}$	Buoyancy force
$\overrightarrow{F_D}$	Stokes drag force
$\overrightarrow{F_{Mag}}$	Magnus lift force
$\overrightarrow{F_{Pg}}$	Pressure gradient force
$\overrightarrow{F_{Saff}}$	Saffman lift force
$\overrightarrow{F_{VM}}$	Virtual mass force
g	Gravitational constant
h_c	Heat transfer coefficient
h_{fg}	Latent heat
$\vec{J}$	Mass diffusion flux in turbulent flow
k	Thermal conductivity
k_c	Mass transfer coefficient
m	Mass
n	Surface normal vector
Nu	Nusselt number
Pr	Prandtl Number
P	Fluid pressure

r	Radius
Re	Reynolds number
S_{ct}	Schmidt number
S_f	Source term of droplet forces
S_H	Source term of evaporation energy
S_m	Source term of evaporating droplet
S_y	Source term of species
T	Temperature
u	Fluid velocity
Y	Local mass fraction of the species

Greek letters

ρ	Fluid density
ρ_p	particle density
μ_t	Turbulent viscosity
λ	Molecular mean free path
$\overline{\overline{\tau}}$	Viscous stress tensor

Abbreviations

AJP	Aerosol jet printing
CFD	Computational fluid dynamics
CVD	Chemical vapor deposition
DI	Deionized water
DRW	Discrete random walk
ITO\PET	Indium tin oxide coated polyethylene terephthalate
LPD	Laser pulsed deposition
PIV	Particle image velocimetry
PVD	Physical vapor deposition
TiO_2	Titanium dioxide

are easily swept away without achieving deposition on the target surface. For overcoming the bow shock phenomenon, nanoparticles in the powder form require additional agglomeration processes to form large enough micro-size particles before cold spraying them [6]. However, most nanomaterials (*e.g.*, nanowires, nanorods) are available in the form of aqueous colloid or suspension that confines the agglomeration process and subsequent cold spraying of these important materials. Alternatively, atomization of these stock nanomaterial solutions into microscale droplets followed by spraying through a supersonic nozzle within a single system could address these problems without a need for

additional material preparation and other time-consuming steps. As schematically given in Fig. 1b, atomized droplets carrying the nano-materials could effectively penetrate the bow-shock zone owing to their higher inertia and momentum gained from the larger size and mass as compared to individual nanoparticles. Moreover, supersonic spraying could lead to improved mechanical adhesion owing to the high impact velocity of nanoparticles. As such, effective deposition of nanomaterials on various surfaces could be achieved by utilizing atomized droplets as the transport medium in a supersonic flow.

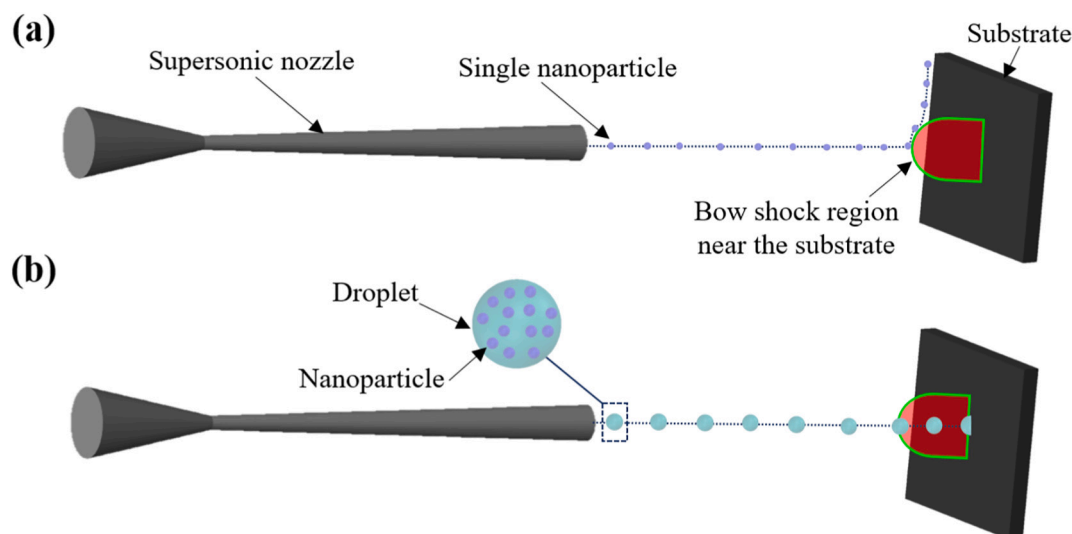More recently, supersonic deposition of nanomaterials from

Fig. 1. Schematic illustration of (a) individual nanoparticle/nanopowder, (b) droplet trajectory under supersonic flow.

atomized droplets has been studied in nanotechnology applications [12–14]. In these studies, some important improvements in the fields of solar cells, thin conductive films, lithium-ion batteries, and self-cleaning films have been achieved owing to the inherent advantages of supersonic spraying including high impact velocity, fast deposition rate, scalability, and cost-effectiveness. As a noteworthy result, self-fused silver nanowires (AgNWs) coating on a transparent conducted film has been achieved with a low sheet resistance through supersonic spraying of AgNWs [15]. In these studies, however, the effect of the continuous phase (gas) on discrete phase (droplet) parameters (*i.e.*, droplet dispersion probability, dispersion morphology, droplet size, droplet temperature, droplet velocity), and the interaction between the phases have not been clearly outlined.

In the last decades, numerous efforts have been made to characterize the supersonic cold spray particle deposition *via* numerical modeling owing to its advantages of speed, accuracy, and reliability [16–20]. These studies contributed to the knowledge of in-flight and deposition characteristics of solid-state microparticles (*i.e.*, size range of 5–50 μm) in supersonic flow. Despite great promises in solid-state cold spraying, the flow behavior (*i.e.*, dispersion probability, dispersion morphology, impact velocity, *etc.*) of liquid-phase droplets under supersonic spraying conditions has not been studied yet extensively. Droplets dynamics under supersonic flow, and their dispersion and deposition characteristics controlled by such above-stated parameters could have a high influence in nanomaterial coating applications in regard to improving deposition process and quality. A better understanding of these phenomena may enable the deployment of supersonically sprayed nanomaterials in wide-range practical applications. Taken together, there is a critical need to understand and elucidate the dispersion and deposition characteristics of the microscale droplets under supersonic spray flow.

In this study, we attempt to address the aforementioned research gaps and challenges by systematically studying the droplets dispersion and deposition characteristics under supersonic flow. First, a numerical model (*i.e.*, two-way coupled discrete phase modeling) for supersonic spraying of droplets was set up to investigate the droplets flow behavior in the continuous gas-phase. To better understand the interaction between the gas phase and the droplets, the influence of the gas phase conditions (*e.g.*, pressure, temperature) on important droplet output parameters (*viz.*, droplet size at deposition, droplet velocity, droplet temperature, droplet dispersion probability, dispersion morphology) is thoroughly studied. The results obtained from numerical modeling are mapped to diagrams in order to provide a generalized parameter window for supersonic cold spraying of droplets, which can help researchers to improve the quality and efficacy of particle deposition. Next, a vacuum-free atomization-based supersonic spray deposition system is developed for model validation, and also to test the adaptability of the developed spray system for nanocoating applications. The findings from the model are experimentally validated by particle image velocimetry (PIV). Furthermore, a case study of titanium dioxide (TiO₂) nanomaterial coating on a polymer surface (*i.e.*, ITO/PET) is performed to demonstrate the proof-of-the-concept of the developed spray system for nanomaterial coating applications.

2. Numerical methodology

In this section, first, the geometry of the supersonic nozzle, and the computational domain are described. Details regarding the continuous phase (gas) and the discrete phase (droplets) are then presented.

2.1. Geometry and computational domain

Numerical simulations of the nozzle flow were performed using the ANSYS-FLUENT V19.1 software to predict the gas flow field and flow characteristics of atomized discrete droplets in the continuous phase. The important nozzle dimensions, computational domain with boundary conditions, and parameters involved in the simulations are

presented in Fig. 2a–b and Table 1, respectively. A two-dimensional axisymmetric model was constructed to reduce computational time. A steady-state pressure-based solver was used considering compressibility effects owing to its common use and well-convergence property in supersonic cold spraying research [21–23]. The flow domain was meshed using the structured elements with 171,150 cells to provide a grid-independent solution. For this cell number, the y^+ value (*i.e.*, non-dimensional distance from the wall to the first mesh node) is obtained as 29.7 for all calculations, which corresponds to a suitable selection criterion for the appropriate mesh and model configuration where the turbulent shear dominates [24]. The flow domain was extended 100 mm axially from the nozzle exit section and 30 mm radially from the nozzle axis to implement the outlet boundary condition and ensure the independence of the solution in the computational domain. A substrate was placed 30 mm away from the nozzle exit location to capture the droplets impact velocity.

Pressure and temperature inlet were specified as the inlet boundary condition. An adiabatic wall with no-slip boundary condition was used at the whole side surfaces of the nozzle and the substrate. The trap boundary condition was defined to the nozzle walls and the substrate to trap the droplets. At the exit of the nozzle and all surrounding boundaries, the outlet pressure boundary condition was applied and set to the atmospheric pressure. The solution was considered converged when the residuals fall below 10^{-6} for the energy equation and 10^{-4} for other equations (*i.e.*, mass, momentum, and turbulence equations).

2.2. Continuous phase – driving gas

The continuous phase was modeled based on the Eulerian approach. The ideal gas law (*i.e.*, $P = \rho RT$) was used to calculate the density changes considering the compressibility effects. The realizable k-ε turbulence model with enhanced wall treatment was used for modeling the turbulence owing to its well acceptance in cold spray research to accurately capture the compressibility effects [25,26]. Further details regarding the realizable k-ε turbulence model can be found in Ref [24]. At the inlet section, the turbulence intensity and turbulent viscosity ratio were set as 5% and 10, respectively. The governing equations of the continuous phase for a steady compressible turbulent flow (neglecting gravitational forces) can be written as follows:

Continuity equation

$$\nabla \cdot (\rho \vec{u}) = S_m \tag{1}$$

Momentum equation

$$\nabla \cdot (\rho \vec{u} \vec{u}) = -\nabla p + \nabla \cdot \overline{\overline{\tau}} + S_f \tag{2}$$

Energy equation

$$\nabla \cdot (\rho e \vec{u}) = -p \nabla \cdot \vec{u} + \nabla \cdot (k \nabla T) + \Phi + S_H \tag{3}$$

Species transport equations

$$\nabla \cdot (\rho \vec{u} Y) = -\nabla \cdot \vec{J} + S_Y \tag{4}$$

$$\vec{J} = -\left(\rho D_m + \frac{\mu_t}{S_{ct}}\right) \nabla Y \tag{5}$$

where, ρ is the gas density, $\vec{u}$ is the velocity, $\overline{\overline{\tau}}$ is the viscous stress tensor, p is the static pressure, e is the specific internal energy, k is the thermal conductivity, T is the temperature, Y is the local mass fraction of the species, $\vec{J}$ is the mass diffusion flux in turbulent flow, and μ_t is the turbulent viscosity. The source terms S_m, S_f, S_H are used to include the contributions of the evaporating species, droplet forces, and evaporation energy from the discrete phase [24]. In addition, S_y is the source term, D_m is the diffusion coefficient for species in the mixture, and S_{ct} is the Schmidt number.
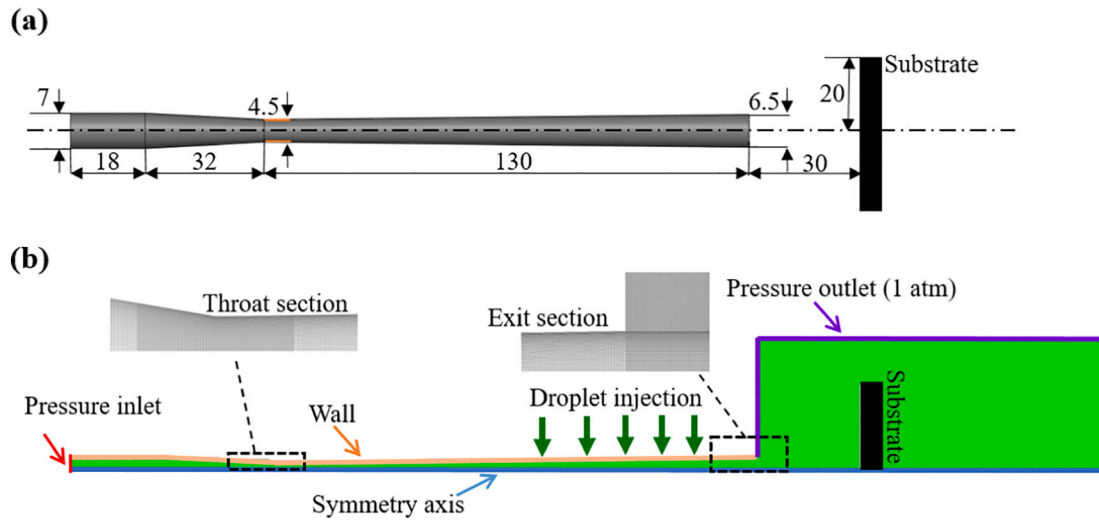
Fig. 2. (a) Schematic of the nozzle geometry, (b) computational domain and boundary conditions (all dimensions are in mm).

Table 1
Parameters involved in the simulations.

Condition	Value/range
Driving gas pressure (MPa)	0.3, 0.4, 0.5, 0.6, 0.7, 0.8,
Driving gas temperature (K)	300, 400, 500, 600
Outlet pressure (atm)	1
Droplet injection position (mm)	130, 140, 150, 160, 170, 180
Droplet size (μm)	0.5, 1, 2, 3, 4, 5, 7.5, 10
Droplet mass flow rate (μg/s)	5

2.3. Discrete phase – droplets

Nanomaterials are generally synthesized as colloids or suspensions using wet-chemical methods. Most of these aqueous solutions have a density similar to water at room temperature (*e.g.*, silver nanoparticles (997 kg/m^3), iron oxide nanoparticles (1000 kg/m^3), *etc.*) [27]. Therefore, in the present numerical study, spherical water droplets are considered as the discrete phase. The amount of solid fraction inside the droplets was neglected in the numerical simulations since the weight fraction of the nanomaterial is significantly less compared to the solvent in the solution. For instance, the weight ratios of some commercial nanoparticle solutions are as follows: 0.5% silver nanowire concentration in isopropyl alcohol suspension, 5% titanium dioxide nanoparticle concentration in ethanol, 5% silica nanoparticles concentration in water [27]. It was assumed that when the droplets are able to reach the target surface, nanomaterial deposition is achieved. Droplet breakup and impingement regimes (*i.e.*, splash, spread, rebound, and stick) are beyond the scope of this present study. Droplet-droplet collisions and possible chemical reactions between the droplets and the continuous phase were neglected in the simulations. The volume fraction of the droplets to continuous phase (air) is smaller than 10%, which makes the use of discrete phase modeling convenient in this study [24].

The droplets were tracked using the Lagrangian scheme. The velocity and trajectory of a droplet were predicted by using Newton's second law:

$$m_d \frac{d\overrightarrow{u_d}}{dt} = \sum \overrightarrow{F} = \overrightarrow{F_D} + \overrightarrow{F_{Ba}} + \overrightarrow{F_{VM}} + \overrightarrow{F_{Pg}} + \overrightarrow{F_{Bu}} + \overrightarrow{F_{Saff}} + \overrightarrow{F_{Mag}} \tag{6}$$

where, $\overrightarrow{u_d}$ is the droplet velocity, ρ_d is the droplet density, $\sum \overrightarrow{F}$ is the sum of hydrodynamic forces, $\overrightarrow{F_D}$ is the Stokes drag force, $\overrightarrow{F_{Ba}}$ is the Basset force (non-steady viscous drag force), $\overrightarrow{F_{VM}}$ is the virtual mass force (inertia of fluid), $\overrightarrow{F_{Pg}}$ is the pressure gradient force, $\overrightarrow{F_{Bu}}$ is the buoyancy force due to pressure distribution on the droplet, $\overrightarrow{F_{Saff}}$ is the Saffman lift

force, and $\overrightarrow{F_{Mag}}$ is the Magnus lift force due to particle rotation [28]. The drag force, Brownian force, and Saffman lift force are considered because the size of the droplets is in the range of 0.5–10 μm, and the density of the continuous phase is significantly lower than the density of the droplets (*i.e.*, $\rho_{air}/\rho_{water} \cong 0.001$). The Stoke's drag law and the corresponding Cunningham slip correction factor are described in Eqs. (7) and (8), respectively. It can be noted that the Stoke's drag law must be corrected by a Cunningham slip correction factor (C_c) for sub-micron particles [29].

$$\overrightarrow{F_D} = \frac{18\mu}{d_p{}^2 \rho_p C_c} \tag{7}$$

$$C_c = 1 + \frac{2\lambda}{d_p} \left[1.257 + 0.4 exp \left(-\frac{1.1 d_p}{2\lambda} \right) \right] \tag{8}$$

where, d_p is the particle diameter, ρ_p is the particle density, λ is the molecular mean free path, and C_c is the Cunningham slip correction factor.

For a droplet having a temperature below the boiling point, the conservation of energy equation can be written as:

$$m_p c_p \frac{dT_p}{dt} = h_c A (T - T_p) + h_{fg} \frac{dm_p}{dt} \tag{9}$$

where, A is the surface area of the droplet, h_{fg} is the latent heat, h_c is the heat transfer coefficient. In Eq. (9), the radiation heat transfer term was neglected because the range of driving gas temperature is low in the divergent section of the nozzle, where the droplets are injected. The evaporation rate of the droplet can be obtained by Eq. (10).

$$\frac{dm_p}{dt} = -A k_c (C_s - C_\infty) \tag{10}$$

where, k_c is the mass transfer coefficient, C_s is the vapor concentration at the droplet surface, C_∞ is the vapor concentration of the bulk flow. The heat and mass transfer coefficients in Eqs. (9) and (10) can be calculated using the following empirical equations [30,31].

$$Nu = 2 + 0.6 Re_p{}^{0.5} Pr^{0.33} \tag{11}$$

$$Sh = 2 + 0.6 Re_p{}^{0.5} S_{ct}{}^{0.33} \tag{12}$$

where, Nu is the Nusselt number, Re is the Reynolds number, Pr is the Prandtl number, Sh is the Sherwood number, and S_{ct} is the Schmidt number respectively.

The influence of the continuous phase on the discrete phase and *vice versa* was studied by two-way coupling of the mass, momentum, and energy equations. A stochastic tracking model, Discrete Random Walk (DRW), was used to analyze the turbulent dispersion and fates of the droplets. The effect of important continuous phase parameters (*i.e.*, driving gas pressure, driving gas temperature) and discrete phase conditions (*i.e.*, droplet size, droplet injection position from nozzle inlet (see Fig. 2)) on droplets' dispersion and deposition characteristics were systematically studied. The studied parameters in the numerical simulations and their values/ranges are listed in Table 2.

3. Numerical results and discussions

This section discusses the droplets dispersion and deposition characteristics onto the target surface under supersonic flow. The effect of continuous phase and discrete phase conditions (see Table 2) on droplet dispersion and deposition characteristics are investigated.

3.1. Effect of inlet gas pressure on droplet velocity

Fig. 3a–b show variation of the droplet velocity along with the axial distance (*i.e.*, position at the nozzle centerline) at different inlet (driving) gas pressures. The droplet size of 3 μm was radially injected into the divergent section of the nozzle at 130 mm to observe the effect of inlet pressure change on the relatively small droplets. Radial injection configuration was selected owing to its cost-effective manufacturing process comparing to axial injection, which needs an extra coaxial injection port. In this analysis, the driving gas and the droplet injection temperatures were considered to be 298 K (*i.e.*, room temperature).

As can be seen in Fig. 3a, inlet gas pressure has a significant impact on droplet acceleration. When the inlet gas pressure is relatively low (*i.e.*, 0.3–0.5 MPa), the droplets velocity sharply decreases around the nozzle's outlet. The reason for this is the existence of normal shock waves inside and outside of the nozzle. As can be seen in Fig. 3b, the spray jet is over-expanded for the inlet gas pressures of 0.3, 0.4, 0.5 MPa, and normal shock waves are formed at the outside of the nozzle. When the inlet gas pressure is further increased (*i.e.*, 0.6, 0.7, 0.8 MPa), the deceleration in the droplets' velocity is not as significant as compared to lower pressure values. This is because of the diminishing effect of the shock waves at the nozzle exit. If a supersonic nozzle is not designed and configured with a proper expanded form for a certain inlet pressure, the flow could experience unwanted shear layers, Mach disks, and compression shocks, which will result in a serious decrease in kinetical energy of the gas flows and coating efficiency [32]. As shown in Fig. 3b, the nozzle design used in this study can perform with a proper expanded flow for the inlet gas pressure of 0.7 MPa (≈100 psi) considering the least shock wave formation observed at the nozzle exit. For this inlet pressure (0.7 MPa), the droplets velocity profile does not experience a significant fluctuation at the nozzle exit as depicted in Fig. 3a. Based on this analysis, the following studies are conducted considering the inlet

Table 2
Studied parameters and their values.

Input parameters	Input values	Output
1) Driving gas pressure (MPa)	[0.3, 0.4, 0.5, 0.6, 0.7, 0.8]	Droplet velocity profile
2) Droplet injection position (mm)	[130, 140, 150, 160, 170, 180]	
3) Droplet size (μm)	[0.5, 1, 2, 3, 4, 5, 7.5, 10]	Droplet dispersion probability Droplet dispersion morphology
4) Driving gas temperature (K)	[300, 400, 500, 600]	Droplet dispersion probability Droplet impact velocity Droplet size Droplet temperature

gas pressure of 0.7 MPa.

3.2. Characteristics of the gas flow field

The characteristics of the nozzle flow are presented in Fig. 4a–f at the driving gas pressure of 0.7 MPa. The contours of the velocity and Mach number distribution are given in Fig. 4a and b, respectively. The flow is correctly expanded with a maximum Mach number of 2.05. Fig. 4c shows the velocity profile along the nozzle axis at different inlet driving gas temperatures. Higher driving gas temperature leads to higher gas velocity. This can be explained by the Mach number equation, $M = u/\sqrt{\gamma R T}$ where M is the Mach number, γ is the adiabatic constant, R is the specific gas constant, and T is the gas temperature. The Mach number does not change significantly at different inlet driving gas temperatures. When the Mach number is kept constant in the formula, the gas velocity is positively proportional to the gas temperature.

The variation of the gas density at different driving gas temperatures is also shown in Fig. 4d. The density decreases with increasing inlet gas temperature due to the ideal gas law. The gas flow field experiences a sharp increase in velocity and decrease in density at 50 mm axial position (*i.e.*, nozzle throat section (see Fig. 2a)) regardless of gas temperature due to the choked flow at the nozzle throat and rapid expansion of the driving gas right after the throat section. In addition, a significant density instability occurs near the substrate independent of the inlet temperature. The reason for this is the rapid compression of the gas near the substrate due to the bow shock, which forms near the substrate as can be seen in Fig. 4e. The bow shock phenomenon is responsible for inherent variation in the flow properties [33].

3.3. Effect of droplet injection position on droplet velocity

The atomization process of nanomaterial solutions is generally carried out near the atmospheric pressure (*e.g.*, ultrasonic atomization, jet atomization). In the supersonic zone (divergent section) of a convergent-divergent nozzle, the static pressure is significantly lower than the inlet chamber due to the expansion of the driving gas from the nozzle throat to exit [34]. This phenomenon allows using of low-pressure feeders like atomizers. In this regard, different droplet injection locations were investigated to observe the effect of injection location on droplet acceleration. The droplets having a diameter of 5 μm were radially injected from different positions of the divergent section at room temperature. As shown in Fig. 5, droplet injection closer to the nozzle exit leads to lower droplet impact velocity. The reason for this is the short accelerating path of the droplets in the nozzle. The droplet impact velocity for the axial injection position of 130 mm is notably higher (*i.e.*, ≅25% more) comparing to the injection position of 180 mm. It can be seen that the droplet injection position has a critical impact on droplet acceleration. In the next sections, the droplet injection position of 130 mm is considered.

3.4. Droplet dispersion probability on the target substrate

This section focuses on the turbulent dispersion of droplets. Droplet dispersion probability on the target surface is investigated for different sizes of droplets from 0.5 to 10 μm and driving gas temperatures. In addition, the dispersion morphology of droplets and their impact velocity onto the substrate are studied.

3.5. Effect of droplet size on dispersion probability

A stochastic tracking model, the Discrete Random Walk (DRW) model, is used to conduct droplet dispersion considering the instantaneous fluctuation of gas velocity. The DRW approach is widely used in the literature for modeling and simulation of particle/droplet dispersion [21,35,36]. A detailed description of the DRW model can be found in Ref
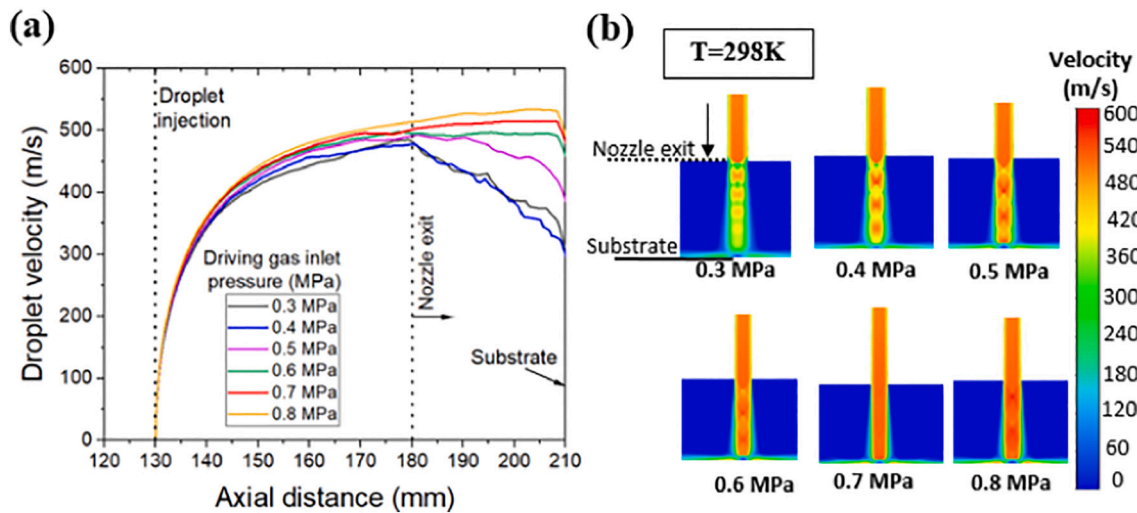
Fig. 3. (a) Effect of inlet (driving) gas pressure on droplet acceleration, (b) contours of the gas velocity outside of the nozzle at different driving gas pressures.

[24]. In the present study, three dispersion probabilities (*i.e.*, droplet fates) have been considered as follows: deposition (*i.e.*, the droplets impact the substrate), escape (*i.e.*, droplets are swept out of the flow domain by the continuous phase), and evaporation (*i.e.*, droplet completely evaporates). For each simulation, the number of injected particle trajectories was increased from 100 to 1000 to test the consistency of the model. Table 3 shows the droplet dispersion probability for different droplet sizes at room temperature. It is observed that the droplets having a diameter of 2 μm or higher more likely can reach the target location and deposition occurs. For 1 μm droplets, the deposition window becomes narrower (57%) with an escape possibility of 38%. There is almost no deposition window for the droplets ≤0.5 μm due to droplet evaporation at near 100%.

3.6. Effect of gas temperature on dispersion probability

Some nanomaterials (*e.g.*, ceramic nanocomposites) generally require high temperature in order to be able to deposit them on the target surface. Driving gas temperature may critically affect droplet dispersion, deposition, and evaporation. In this regard, it is critical to study the effect of driving gas temperature for droplets flow characterization including droplet dispersion and deposition parameters. This subsection conveys the effect of driving gas temperature on dispersion probability. In the next sections (*i.e.*, Sections 3.5–3.7) the effect of driving gas temperature on critical droplets deposition parameters (*i.e.*, droplet impact velocity, droplet size, droplet temperature) are investigated.

Table 4 presents the droplets dispersion probability at different driving gas temperatures ranging from 400 K to 600 K. Deposition occurs at all the given inlet gas temperatures for the droplets larger than 2 μm. However, the deposition rate of 2 μm droplets significantly decreases (%32) at the inlet gas temperature of 600 K while there is no deposition window for the droplets ≤1 μm after 500 K gas temperature. The results show that smaller droplets are more susceptible to evaporation at elevated driving gas temperatures.

3.7. Effect of droplet size on dispersion morphology and impact velocity

Fig. 6a shows the radial position (*i.e.*, upon impact to the substrate) and corresponding impact velocities for different sizes of droplets at room temperature. The droplet dispersion behavior is observed to be dissimilar for different droplet sizes. The larger droplets (*i.e.*, 3–10 μm) follow a straight trajectory and impact the target surface within a narrower region (about 2.5 mm radius of the nozzle central axis). In

contrast, the smaller droplets (≤2 μm) spread and scatter more in the radial direction over the substrate surface. A reason for this phenomenon can be that larger droplets have sufficient momentum to maintain straight flight and the effect of turbulence is not dominant on these droplets. Conversely, the effect of turbulence on particle trajectory is more dominant for smaller droplets [18]. Another reason for such behavior could be the bow shock near the substrate. The smaller size droplets (≤2 μm) cannot easily penetrate the bow shock due to their relatively low inertia and momentum, and their trajectories are severely affected resulting in more dispersion onto the target surface [9,33]. Another finding from Fig. 6a is that the impact velocity decreases with increasing droplet diameter for a certain range of droplet size (*i.e.*, 4–10 μm). This is likely attributed to the higher drag force and inertia of the larger droplets [37]. Conversely, the trend is different for the smaller droplets ≤3 μm, which have less impact velocity than the larger droplets. Fig. 6b shows the average impact velocity of droplets with standard deviations. As can be seen, the standard deviation in the impact velocity of the droplets ≤2 μm is significantly higher as compared to larger droplets. The reason for this is the high dispersive behavior of the smaller droplets onto the target surface as presented in Fig. 6a.

3.8. Effect of driving gas temperature on droplet impact velocity

Fig. 7a shows the droplet impact velocity diagram for variation of droplet size and driving gas temperature. The first finding from the figure is that the higher driving gas temperatures result in higher droplet impact velocity for the droplets ≥2 μm. The results are in agreement with the experimental studies in the literature, in which the spray deposition of particles at different stagnation temperatures was investigated [38,39]. However, there is no deposition window for the droplets ≤0.5 μm at all given temperatures, and 1 μm droplets evaporate completely after 400 K. The second finding is that the impact velocity of droplets in the size range of 3–7 μm increases significantly with increasing driving gas temperature, whereas the increase in impact velocity of larger droplets (>7 μm) is not as prominent as smaller droplets. The reason for this could rely upon the insufficient internal energy gain of the driving gas at elevated temperatures to accelerate larger droplets (*i.e.*, droplets with higher inertia).

3.9. Effect of inlet gas temperature on droplet size

Fig. 7b shows the contour plot of droplet size at the impingement *versus* inlet gas temperature and initial droplet size. As can be seen, an increase in the driving gas temperature prompts a decrease in the
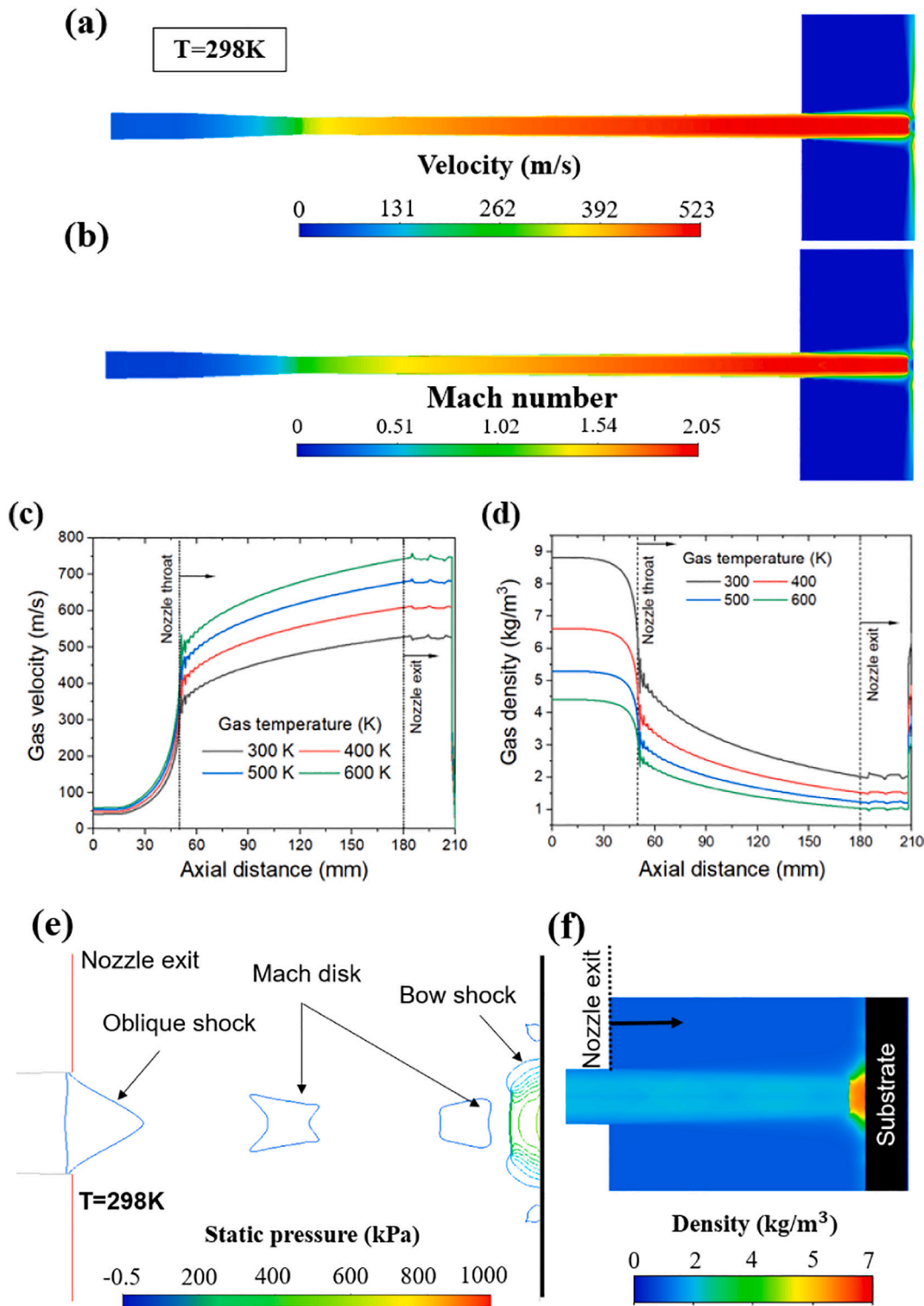
Fig. 4. (a) Velocity and (b) Mach number distribution inside and outside of the nozzle, (c) gas velocity along the nozzle axis at different inlet temperatures, (d) variation of the gas density with gas inlet gas temperature, (e) contour of the gas pressure at the nozzle exit, (f) contour of gas density at the nozzle exit.

droplet size. This result matches well with the studies [40,41], which revealed that an increase in the temperature of the gaseous medium leads to a higher droplet evaporation rate. Moreover, the rate of droplet size change varies with respect to the initial droplet size. Particularly, smaller droplets (*i.e.*, 0.5–2 μm) are more susceptible to evaporation. This result agrees with the d^2-law of droplet evaporation that formulates that the evaporation time of a droplet decreases with the decreasing

droplet size [37]. The size change of the droplets ≥ 3 μm is not as remarkable as smaller droplets. All the droplets ≥ 3 μm can reach the substrate surface without complete evaporation.

3.10. Effect of inlet gas temperature on droplet temperature

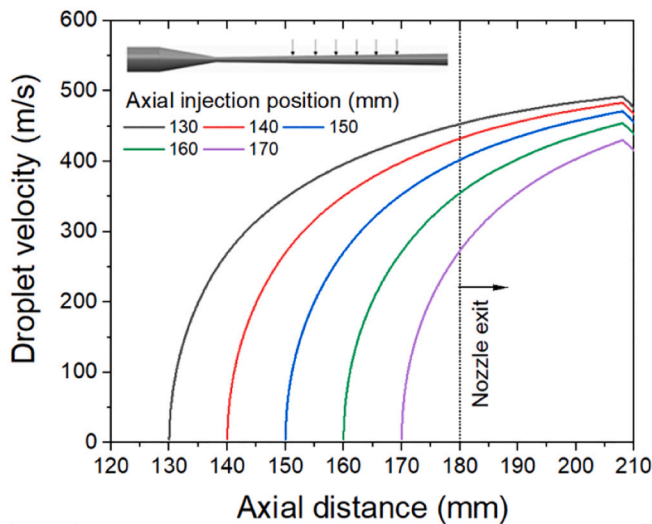Fig. 7c shows the droplets impingement temperature for different

Fig. 5. Droplet velocity profile along the centerline for different injection positions.

Table 3
Droplet dispersion probability at room temperature.

Number of droplet trajectories	Droplet size (µm)	Deposition (%)	Escape (%)	Evaporation (%)
100, 500, 1000	10	100.0	0.0	0.0
100, 500, 1000	7.5	100.0	0.0	0.0
100, 500, 1000	5	100.0	0.0	0.0
100, 500, 1000	4	100.0	0.0	0.0
100, 500, 1000	3	100.0	0.0	0.0
100, 500, 1000	2	99.0, 99.0, 99.5	1.0, 1.0, 0.5	0.0
100, 500, 1000	1	55.0, 57.0, 60.8	39.0, 38.8, 35.9	6.0, 4.2, 3.3
100, 500, 1000	0.5	1.0, 2.6, 2.1	0.0	99.0, 97.4, 97.9

droplet sizes and driving gas inlet temperatures. Also, Fig. 7d shows the variation of driving gas temperature along the nozzle axis. An important finding from Fig. 7c is that higher driving gas temperatures result in increased droplet temperature due to the interaction between the continuous phase and droplets. For all the inlet gas temperatures, the droplet temperature is under the boiling point so that the mass change of the droplets is primarily determined by the evaporation. The reason for this is the significant temperature drop of the gas flow in the divergent section of the nozzle due to the rapid expansion of gas. As shown in Fig. 7d, the driving gas (air) experiences a remarkable temperature drop when it flows through the divergent zone, leading to an important decrease in droplet temperature. The result is comparable with the literature that has reported the particle impact temperature is remarkably lower when the particles are injected from the divergent section of

the nozzle [42].

4. Experimental validation and case study

This section describes the experimental spray setup and methodology for the validation of the numerical modeling. In addition, a case study is carried out using commercial titanium dioxide (TiO_2) nanopowders to confirm the feasibility of the described spray deposition system for nanomaterial coating applications.

4.1. Experimental setup and procedure

The convergent-divergent nozzle described in Section 2.1 was manufactured by wire electrical discharge machining. The vacuum-free atomization-based supersonic spray deposition system was developed and used in the coating experiments. The spray system includes two separate modules of the supersonic nozzle and decoupled atomization unit. Through the decoupled atomization process setup depicted in Fig. 8a, the liquid nanomaterial solutions (*i.e.*, suspension or colloid) are atomized in a separate atomization chamber to obtain a better control on the droplet size distribution before spraying. The atomized droplets are then carried to the injection port of the nozzle through the low-velocity carrier gas flow. As such, the decoupled atomization enables a better deposition control on the spraying process by allowing to configure the droplets' mass flow rate and injection velocity [43]. The schematic of the spray system and the image of the experimental setup are presented in Fig. 8a and b, respectively.

The spray setup consists of the supersonic nozzle, the pneumatic jet atomizer (WestMed-0210 VixOne), high-pressure driving gas inlet, and low-pressure carrier/atomizer gas inlet. Compressed air without preheating was used as the driving gas and the droplet carrier gas. In the TiO_2 nanomaterial coating experiments, the nozzle was mounted on a 3-axis computer numerical controlled (CNC) framework to precisely control the spraying process.

The spray process, as shown in Fig. 8a, begins with the atomization of the nanomaterial solution in the atomizer chamber. The atomized microscale droplets are carried to the nozzle and then radially injected into the divergent section by the low-pressure carrier gas flow. Then, the high-pressure central gas flow accelerates the droplets to supersonic velocities achieving nanomaterial deposition onto the target surface. The spray parameters used in the experiments are listed in Table 5.

To validate the CFD predictions, a particle image velocimetry (PIV) system was used to measure the in-flight droplet flow behavior and their velocity values. The spray parameters were used as listed in Table 5 by considering the spray distance of 50 mm for both CFD simulations and PIV measurements to observe a longer downstream of the spray. As shown in Fig. 8c, in the PIV setup, two laser pulses from a dual-head, Nd: YAG pulse laser (wavelength 532 nm, maximum energy of 200 mJ per pulse, pulse length of 5 ns) were spanned into a light sheet by a group of optical lenses to illuminate the spray flow-field with a time interval of $\Delta t = 1$ ns. A 1600 × 1200 pixels charge-coupled device (CCD) camera was positioned normal to the light sheet and synchronized to record
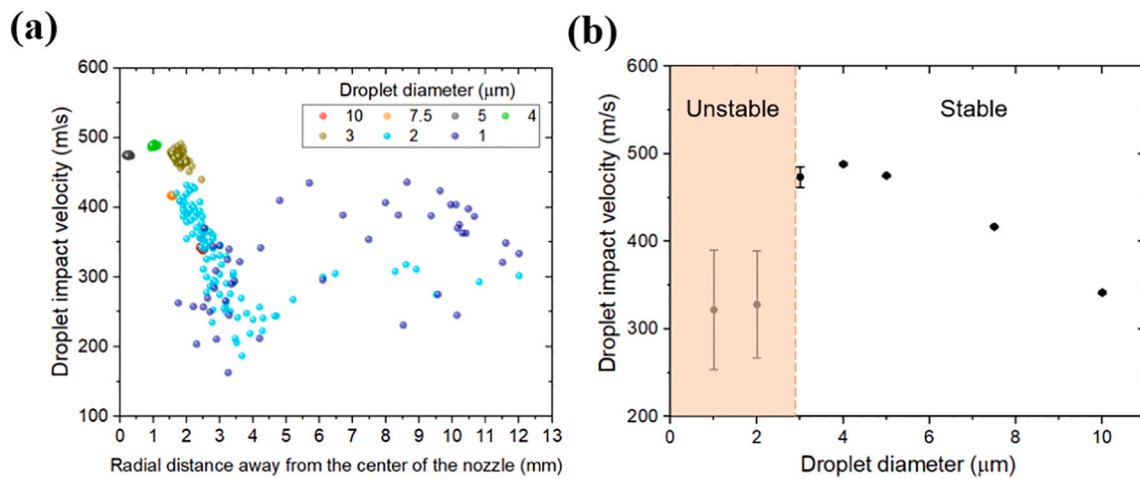
Table 4
Droplet dispersion probability at different driving gas temperatures.

Droplet size (µm)	Temperature								
	400 K			500 K			600 K		
	Deposition (%)	Escape (%)	Evaporation (%)	Deposition (%)	Escape (%)	Evaporation (%)	Deposition (%)	Escape (%)	Evaporation (%)
10	100.0	0.0	0.0	100.0	0.0	0.0	100.0	0.0	0.0
7.5	100.0	0.0	0.0	100.0	0.0	0.0	100.0	0.0	0.0
5	100.0	0.0	0.0	100.0	0.0	0.0	100.0	0.0	0.0
4	100.0	0.0	0.0	100.0	0.0	0.0	100.0	0.0	0.0
3	100.0	0.0	0.0	100.0	0.0	0.0	100.0	0.0	0.0
2	99.0	1.0	0.0	91.0	3.0	6.0	32.0	0.0	68.0
1	19.0	2.0	79.0	0.0	0.0	100.0	0.0	0.0	100.0

Fig. 6. (a) Droplet dispersion over the substrate surface against the radial position (b) droplet impact velocity with respect to droplet diameter.
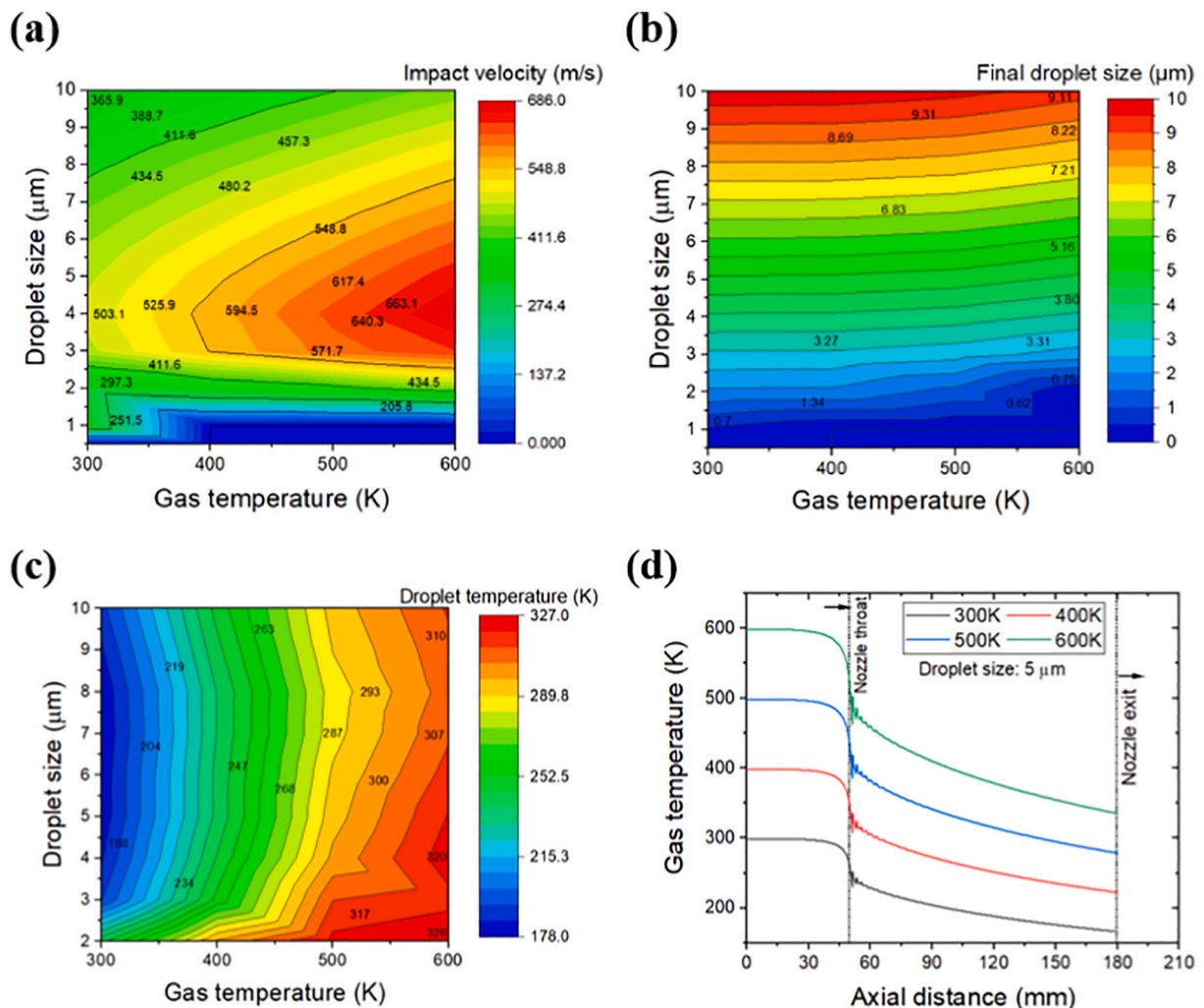

Fig. 7. Diagrams of (a) droplet impact velocity (b) droplet size, (c) droplet temperature for variation of droplet size and gas temperature; (d) temperature profile of the driving gas along the nozzle axis.

droplet images illuminated by the two consecutive laser pulses on a single camera exposure. The imaging resolution (*i.e.*, effective physical size resolved by a single-pixel through the camera lens) is 46.1 µm. The PIV measurement was repeated at 2 Hz and a total of 2000 double-exposed images were recorded.

The droplets velocity data were extracted from the recorded images using a PIV analysis software (Davis 8.4). The double-exposed images were analyzed using the auto-correlation algorithm with an initial
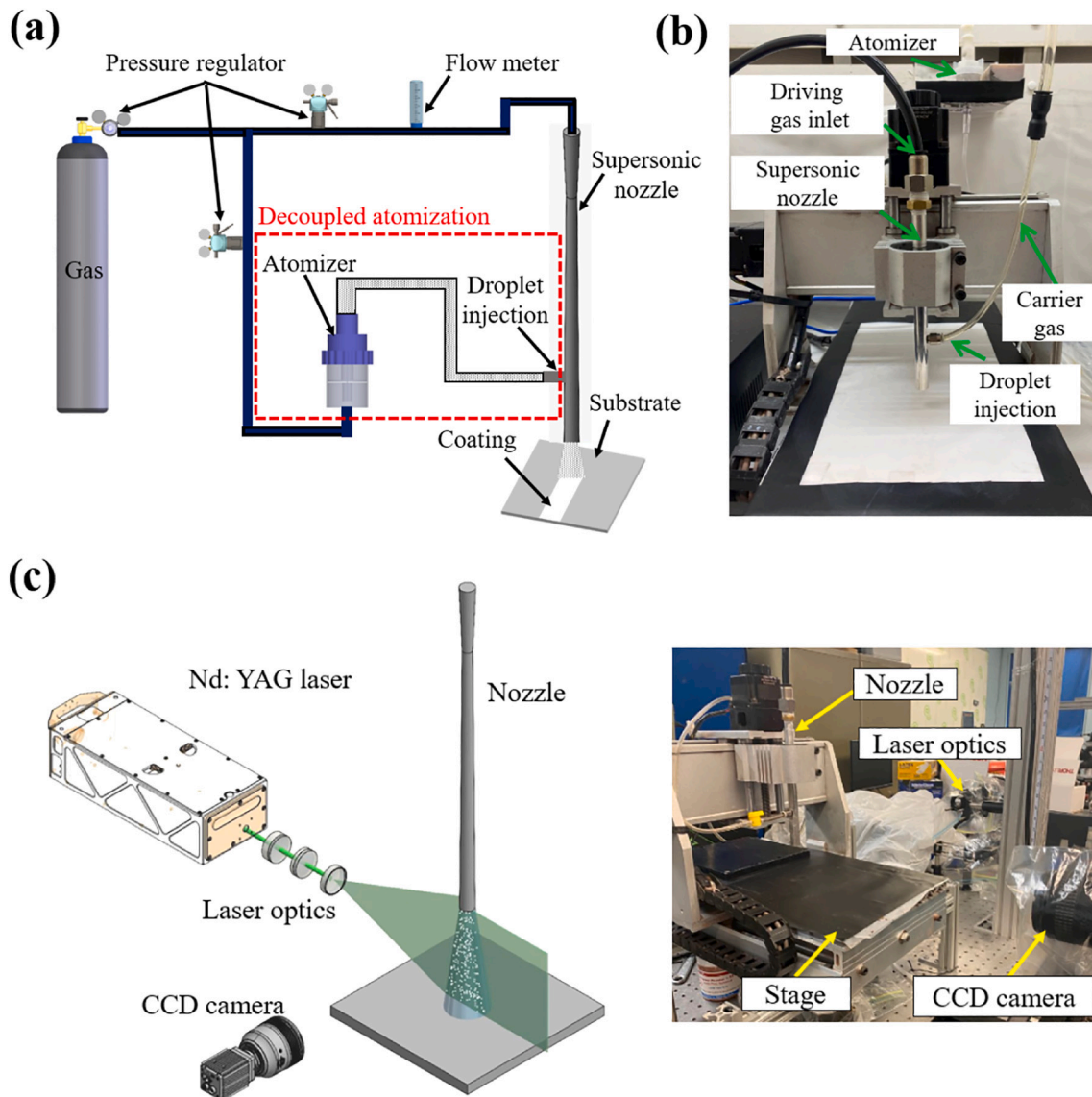
Fig. 8. (a) Schematic of the spray deposition system, (b) image of the experimental setup, (c) experimental setup for PIV measurement.

Table 5
Spray parameters.

Process parameters	Value
Driving gas	Air
Driving gas inlet pressure (MPa)	0.7
Driving gas inlet temperature (K)	298
Atomization pressure (kPa)	70
Nozzle stand-off distance (mm)	30, 50
Droplet injection position from nozzle inlet (mm)	130

window size of 128×128 pixels and 50% overlap that iterates for three times, and then 32×32 pixels window with 50% overlap that iterates twice. The average droplet displacement, Δx, was identified in each window with a correlation value larger than 0.25. A clear picture of the sprayed droplet stream (see Fig. 9c) was obtained by averaging 2000 images, and the velocity vectors were then calculated by $u = \Delta x/\Delta t$ and plotted from these data.

4.2. Validation and discussion

In numerical simulations, a droplet stream was injected into the nozzle divergent section, the trajectories of the droplets were then tracked. The droplet diameters were best described by the Rosin-Rammler size distribution:

$$Y_d = e^{-\left(d/\bar{d}\right)^n} \tag{13}$$

where, d is the droplet diameter, $\bar{d}$ is the mean droplet diameter, n is the size distribution parameter, and Y_d is the mass fraction of droplets. The size distribution parameters were applied to the model by considering the atomizer's technical specifications, which can be found in Ref [44].

The dispersion behavior of water droplets was analyzed by examining the recorded images and then compared with the simulation outputs. Fig. 9a shows a CCD image of the impinging sprayed droplets, and Fig. 9b presents the droplets' velocity trajectories at the nozzle exit obtained from numerical simulations. Both figures indicate that the droplets experience a significant dispersion near the substrate, attributing to the compression waves due to the flow compressibility near the substrate. The compression waves are responsible for a high-density region (*i.e.*, as shown in Fig. 4f) close to the substrate and disrupt the center-periphery of droplets by propagating the formation of lateral jets [45]. In addition, the smaller droplets disperse much in radial direction near the target surface (Supplementary Fig. 1a) comparing to larger
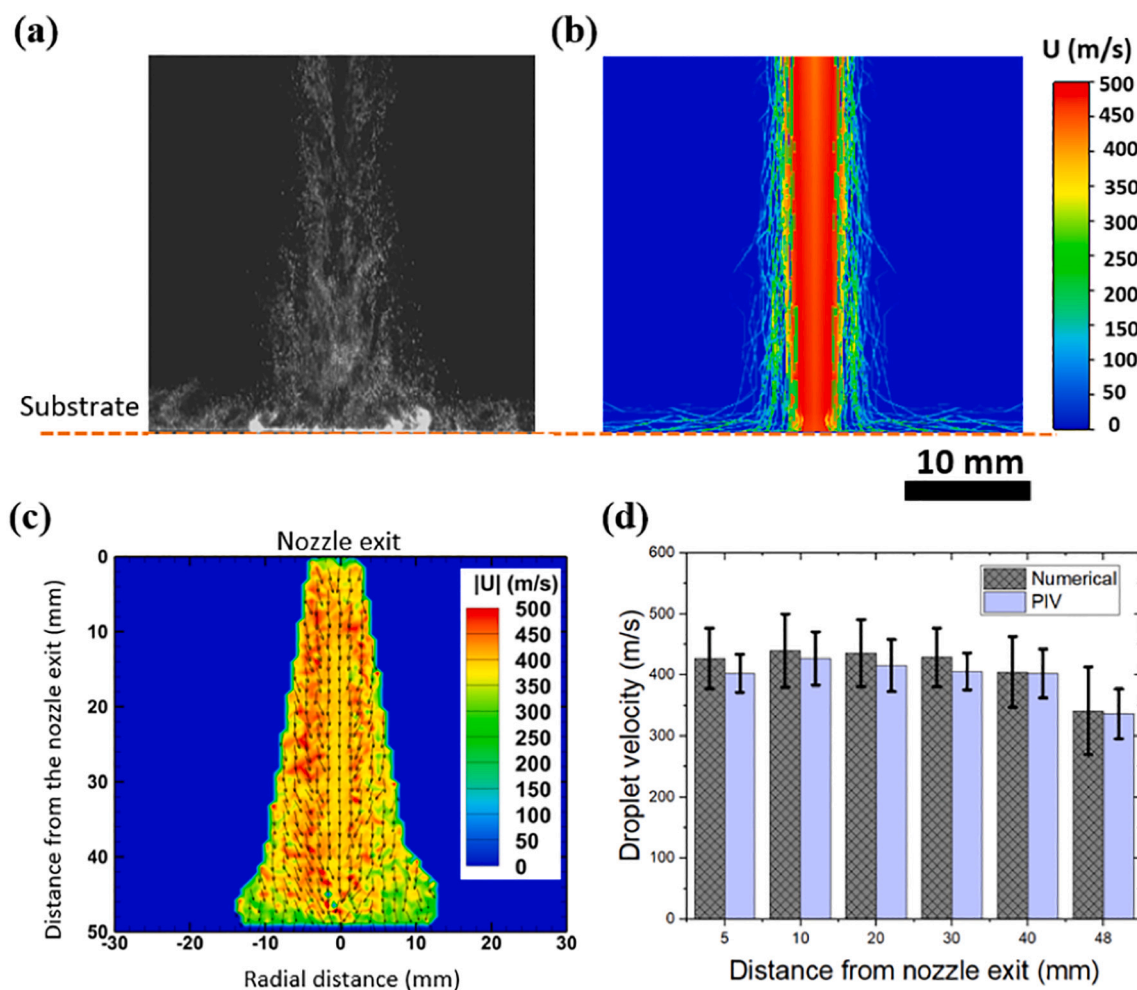
Fig. 9. (a) A CCD camera image of sprayed droplets, (b) velocity distribution of the droplets estimated by the numerical model, (c) PIV-measured velocity of the droplets (|U| denotes the velocity magnitude), (d) comparison of PIV-measured droplet velocity with the numerical model.

droplets. This result is also comparable with the numerical simulations (see Fig. 6a and Supplementary Fig. 1).

The droplets velocity was also compared from both CFD simulations and PIV measurements along the radial (lateral) direction of the nozzle exit at different downstream distances (*i.e.*, 5, 10, 20, 30, 40, and 48 mm away downstream of the nozzle). The measured droplets velocity values were averaged, and the standard deviation was calculated to compare the numerical simulation results with PIV measurements. Fig. 9c shows the PIV image of the velocity vector field and the velocity magnitude (| U|) of the droplets from the nozzle exit to the downstream of 48 mm. Fig. 9d compares the PIV measurements and numerical modeling results for droplets velocity. Both simulation predictions and PIV measurements show a similar trend in droplet velocity. The numerical modeling calculated the droplets velocity slightly higher (*i.e.*, $\cong$ 5% for average values) than the PIV results with a higher standard deviation. This is likely attributed to the absence of the more accurate droplet injection port in the computational domain. The use of point injection for droplets could lead to this error in the simulations. Another possible reason could be the two-dimensional axisymmetric assumption in the modeling.

Another important finding from PIV measurements is that the velocity of droplets near the center of the jet is less than the outer central regions. The reason for this can be attributed to the aggregation of the larger droplets at the center of the jet (Supplementary Fig. 1a). Larger droplets (*i.e.*, $\geq$5 μm) should have enough inertia to reach the center of the jet after their injection into the nozzle. On the other hand, the smaller droplets (*i.e.*, <5 μm), are captured by the gas flow near the

inner wall regions. As such, the larger droplets experience low velocities near the central region of the jet (Supplementary Fig. 1b).

Besides, the velocity of droplets decreases significantly near the substrate. This is likely attributed to the gradual decrease of the jet velocity next to the impinging point (*i.e.*, stagnation point). This phenomenon can also be seen from numerical simulations (see Fig. 4c). The small (*i.e.*, microscale) droplets usually follow the jet flow faithfully thus experience a deceleration in velocity near the target surface. However, due to enough inertia and momentum of larger droplets (*i.e.*, 3 μm or larger, refer Fig. 6), they can travel straight and can penetrate the bow shock region for successful deposits onto the target surface. Overall, the numerical simulations agree well with the PIV experiments and captured similar trends of flow behavior for the supersonically sprayed droplets.

4.3. Case study on TiO₂ nanomaterial coating

In this section, the results observed in the numerical approach (Section 4.1) and experimental validation (Section 4.2) are further validated *via* a case study on nanomaterial coating from atomized droplets. The case study is also aimed to test the supersonic spray system shown in Fig. 8a–b for nanocoating applications. In this regard, a titanium dioxide (TiO_2) solution made of TiO_2 nanocrystalline powders (Nanoamor, USA, anatase phase, average particle diameter of 10 nm) was prepared to be atomized and then sprayed onto indium tin oxide coated polyethylene terephthalate (ITO/PET) substrate at room temperature. TiO_2 nanoparticles were selected as the feedstock material

owing to their many applications in self-cleaning, antibacterial coating, and dye-sensitized solar cell [32]. Despite great promises, the current methods for coating TiO_2 nanoparticles from paste on ITO/PET polymer surfaces, such as doctor blading [46] and spin coating [47] are very challenging and yet inadequate. The final coatings obtained by using these techniques generally suffer from crack and porosity [48]. Moreover, the TiO_2 pastes generally include surfactant and binder materials, which require to be removed by heat treatment at higher temperatures, but ITO/PET can only be cured at a temperature lower than 150 °C due to its low glass transition temperature [48]. As such, a deposition method that enables the binder and surfactant-free coating of TiO_2 nanoparticles (*i.e.*, mixed/diluted with ethanol or water) on the ITO/PET surface is highly needed.

As stated above, we utilized the described supersonic spray deposition system developed in our lab to address these important challenges, and also highlight the numerical modeling results as a nanocoating application. Fig. 10a shows the Scanning Electron Microscopy (SEM, Hitachi S-4800) image of the TiO_2 powders used in the experiments. The solvent-based TiO_2 solution was prepared by vigorously mixing 12.5 mg/mL of TiO_2 nanopowders with 4 mL of DI water and 37.5 mL of ethanol to a total solution volume of 40 mL. It can be noted that the pneumatic jet atomizers can enable to atomize the nanomaterial solutions having a viscosity range of 1–1000 cp [49]. The concentration of the nanomaterial solutions can be determined considering this viscosity range. The deposition of the droplets carrying the TiO_2 nanoparticles was carried out using the spray parameters provided in Table 5. The nozzle speed and stand-off distance were set to be 20 mm/min and 30 mm, respectively. One spray pass was implemented in the coating experiment.

Fig. 10b shows the surface morphology of the resultant TiO_2 coating on the substrate surface. Micrometer-sized-scale TiO_2 coating on the PET surface was achieved under vacuum-free conditions using the described deposition method. Moreover, no crack has been observed in the coating. The surface morphology achieved from the TiO_2 coating is comparable with the TiO_2 deposited substrate obtained by the vacuum

cold spraying method [50]. Besides, it is also observed that the central region of the coating is denser than the outer regions. This is likely attributed to the existence of the larger droplets at the center of the spray jet as observed in the numerical simulations (see Supplementary Fig. 1). Moreover, based on the numerical simulations, the droplets of <3 μm disperse more onto the substrate surface (see Fig. 6a) while the larger droplets (≥3 μm) impact on the substrate in a more focused manner (*i.e.*, near the central axis), which could suggest another potential reason for the coating morphology in Fig. 10b. Fig. 10c shows the cross-sectional morphology of the TiO_2 coating. The resultant coating has an average thickness of 60 μm. Fig. 10d presents the optical profilometer (Zygo, Newview) image of the resultant coating. The coating has an average roughness (Sa) of 0.397 μm and root mean square roughness (Sq) of 0.551 μm. These results suggest that the described atomization-based supersonic spray setup has the potential to overcome the current limitations in TiO_2 nanoparticle coating on ITO/PET polymer substrate.

5. Conclusion

The droplet deposition and dispersion characteristics under supersonic flow were systematically studied by numerical simulations. The effect of driving gas properties, droplet injection location, and droplet size on important droplet parameters were investigated. An atomization-based supersonic spray deposition system was developed and used in the experimental studies. PIV measurements were performed to validate the numerical modeling results. A case study was also conducted to show the applicability of the described spraying approach in nanomaterial coating applications. The following conclusions can be drawn from the present study:

- Supersonic spray deposition of nanomaterial solutions could be achieved by utilizing the atomized droplets as the transport medium.
- The velocity of the smaller droplets (*i.e.*, ≤3 μm) is significantly affected by the normal shock waves formed inside and outside of the
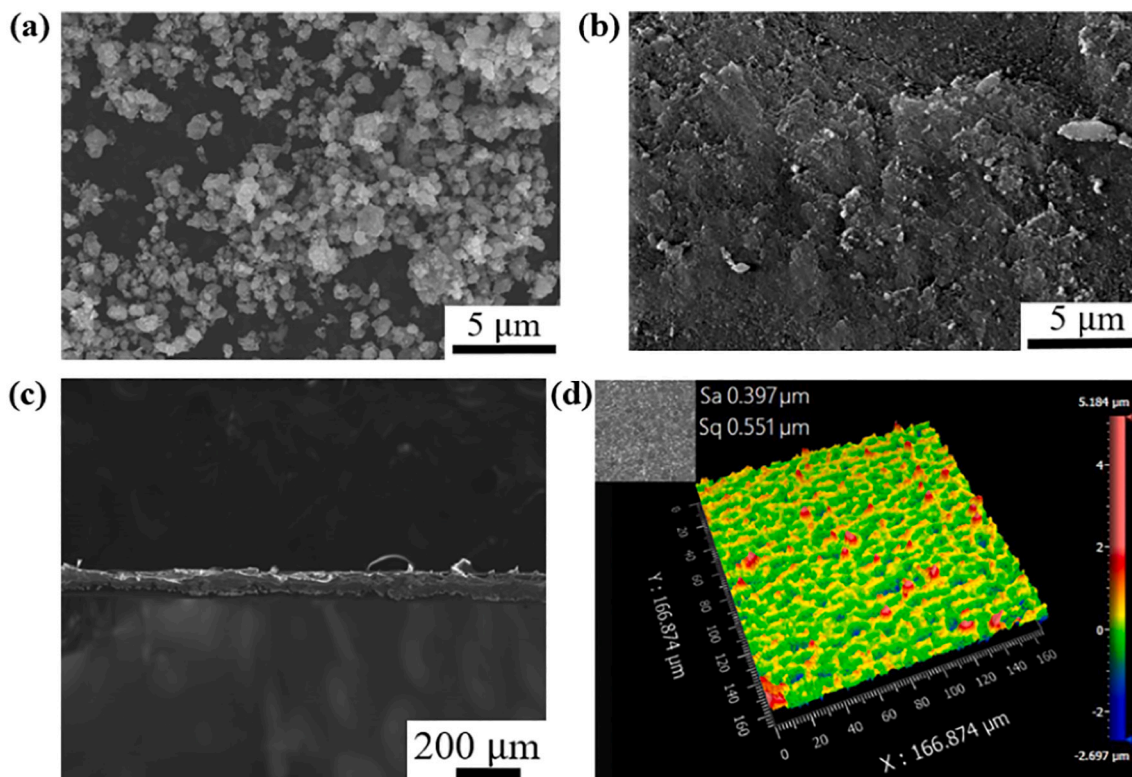

Fig. 10. (a) Morphology of TiO_2 powders, (b) surface SEM image of the coating, (c) cross-section SEM image of the coating, (d) surface profile of the coating.

nozzle. Therefore, the nozzle expansion ratio should be optimized for a certain inlet gas pressure when dealt with smaller droplets.

- The bow shock region near the substrate critically influences the droplets' velocity profile and dispersion of smaller droplets.
- The droplet injection location has an important impact on droplet acceleration. Injecting droplets nearer to the nozzle exit line results in lower droplet impact velocity due to the short acceleration path.
- The droplets of <2 μm are more susceptible to turbulent dispersion and evaporation than the larger droplets.
- Droplet temperature and evaporation rate increase with increasing driving gas temperature.
- The presented atomization-based supersonic spray deposition system could be successfully used in nanomaterial coating applications.
- The numerical simulations, the experimental PIV measurements, and the case study on TiO_2 nanoparticle coating reveal that nanomaterial solutions can be successfully deposited on the target surface by utilizing a supersonic spray system integrated with the decoupled nanomaterial atomization process.

Supplementary data to this article can be found online at https://doi.org/10.1016/j.surfcoat.2021.127788.

CRedit authorship contribution statement

Semih Akin: Conceptualization, design, simulation, experiments, characterization, testing, manuscript preparation.
Puyuan Wu: PIV measurements, manuscript preparation.
Jung-Ting Tsai: Microstructure characterization.
Chandra Nath: Conceptualization, supervision, writing-review & editing.
Jun Chen: PIV measurements, supervision, review & editing.
Martin Byung-Guk Jun: Conceptualization, supervision, review & editing.
All authors commented on the paper.

Declaration of competing interest

The authors declare that they have no known competing financial interests or personal relationships that could have appeared to influence the work reported in this paper.

Acknowledgements

References

[1] X. Zhao, C. Wei, Z. Gai, S. Yu, X. Ren, Chemical vapor deposition and its application in surface modification of nanoparticles, Chem. Pap. 74 (2020) 767–778, https://doi.org/10.1007/s11696-019-00963-y.
[2] C.E. Cross, J.C. Hemminger, R.M. Penner, Physical vapor deposition of one-dimensional nanoparticle arrays on graphite: seeding the electrodeposition of gold nanowires, Langmuir. 23 (2007) 10372–10379, https://doi.org/10.1021/la7016209.
[3] D. Verma, A. Ranga Rao, V. Dutta, Surfactant-free CdTe nanoparticles mixed MEH-PPV hybrid solar cell deposited by spin coating technique, Sol. Energy Mater. Sol. Cells 93 (2009) 1482–1487, https://doi.org/10.1016/j.solmat.2009.03.030.
[4] R.A. Ganeev, U. Chakravarty, P.A. Naik, H. Srivastava, C. Mukherjee, M.K. Tiwari, R.V. Nandedkar, P.D. Gupta, Pulsed laser deposition of metal films and nanoparticles in vacuum using subnanosecond laser pulses, Appl. Opt. 46 (2007) 1205–1210, https://doi.org/10.1364/AO.46.001205.
[5] T. Seifert, E. Sowade, F. Roscher, M. Wiemer, T. Gessner, R.R. Baumann, Additive manufacturing technologies compared: morphology of deposits of silver ink using inkjet and aerosol jet printing, Ind. Eng. Chem. Res. 54 (2015) 769–779, https://doi.org/10.1021/ie503636c.
[6] W. Li, H. Assadi, F. Gaertner, S. Yin, A review of advanced composite and nanostructured coatings by solid-state cold spraying process, Crit. Rev. Solid State Mater. Sci. 44 (2019) 109–156, https://doi.org/10.1080/10408436.2017.1410778.
[7] S. Yin, C. Chen, X. Suo, R. Lupoi, Cold-sprayed metal coatings with nanostructure, Adv. Mater. Sci. Eng. 2018 (2018), https://doi.org/10.1155/2018/2804576.
[8] R.S. Lima, J. Karthikeyan, C.M. Kay, J. Lindemann, C.C. Berndt, Microstructural characteristics of cold-sprayed nanostructured WC-Co coatings, Thin Solid Films 416 (2002) 129–135, https://doi.org/10.1016/S0040-6090(02)00631-4.
[9] T.C. Jen, L. Li, W. Cui, Q. Chen, X. Zhang, Numerical investigations on cold gas dynamic spray process with nano- and microsize particles, Int. J. Heat Mass Transf. 48 (2005) 4384–4396, https://doi.org/10.1016/j.ijheatmasstransfer.2005.05.008.
[10] V. Champagne, D. Helfritch, The unique abilities of cold spray deposition, Int. Mater. Rev. 61 (2016) 437–455, https://doi.org/10.1080/09506608.2016.1194948.
[12] S. An, B. Joshi, A.L. Yarin, M.T. Swihart, S.S. Yoon, Supersonic cold spraying for energy and environmental applications: one-step scalable coating technology for advanced micro- and nanotextured materials, Adv. Mater. 32 (2020), 1905028, https://doi.org/10.1002/adma.201905028.
[13] H.S. Jo, S. An, C.W. Park, D.Y. Woo, A.L. Yarin, S.S. Yoon, Wearable, stretchable, transparent all-in-one soft sensor formed from supersonically sprayed silver nanowires, ACS Appl. Mater. Interfaces 11 (2019) 40232–40242, https://doi.org/10.1021/acsami.9b12847.
[14] H. Choi, J.G. Lee, X.D. Mai, M.C. Beard, S.S. Yoon, S. Jeong, Supersonically spray-coated colloidal quantum dot ink solar cells, Sci. Rep. 7 (2017) 1–8, https://doi.org/10.1038/s41598-017-00669-9.
[15] J.G. Lee, D.Y. Kim, J.H. Lee, S. Sinha-Ray, A.L. Yarin, M.T. Swihart, D. Kim, S.S. Yoon, Production of flexible transparent conducting films of self-fused nanowires via one-step supersonic spraying, Adv. Funct. Mater. 27 (2017), 1602548, https://doi.org/10.1002/adfm.201602548.
[16] S. Garmeh, M Jadidi, A Dolatabadi, Three-dimensional modeling of cold spray for additive manufacturing, J. Therm. Spray Technol. 29 (n.d.). doi:https://doi.org/10.1007/s11666-019-00928-3.
[17] K. Harihara Sudhan, G. Krishna Prasad, N.K. Kothurkar, A.R. Srikrishnan, Studies on supersonic cold spray deposition of microparticles using a bell-type nozzle, Surf. Coat. Technol. 383 (2020), https://doi.org/10.1016/j.surfcoat.2019.125244.
[18] S. Yin, Q. Liu, H. Liao, X. Wang, Effect of injection pressure on particle acceleration, dispersion and deposition in cold spray, Comput. Mater. Sci. 90 (2014) 7–15, https://doi.org/10.1016/j.commatsci.2014.03.055.
[19] S. Yin, X. fang Wang, W. ya Li, Computational analysis of the effect of nozzle cross-section shape on gas flow and particle acceleration in cold spraying, Surf. Coat. Technol. 205 (2011) 2970–2977, https://doi.org/10.1016/j.surfcoat.2010.11.002.
[20] B. Samareh, O. Stier, V. Lüthen, A. Dolatabadi, Assessment of CFD Modeling via Flow Visualization in Cold Spray Process, (n.d.). doi:https://doi.org/10.1007/s11666-009-9363-9.
[21] R. Lupoi, W. O'Neill, Powder stream characteristics in cold spray nozzles, Surf. Coat. Technol. 206 (2011) 1069–1076, https://doi.org/10.1016/j.surfcoat.2011.07.061.
[22] A. Sova, A. Okunkova, S. Grigoriev, I. Smurov, Velocity of the particles accelerated by a cold spray micronozzle: experimental measurements and numerical simulation, J. Therm. Spray Technol. 22 (2013) 75–80, https://doi.org/10.1007/s11666-012-9846-y.
[23] R. Lupoi, Current design and performance of cold spray nozzles: experimental and numerical observations on deposition efficiency and particle velocity, Surf. Eng. 30 (2014) 316–322, https://doi.org/10.1179/1743294413Y.0000000214.
[24] ANSYS Fluent 12.1 User Guide, No Title, 2011.
[25] C. Singhal, Q. Murtaza, P. Parvej, Simulation of critical velocity of cold spray process with different turbulence models, Mater. Today Proc. 5 (2018) 17371–17379, https://doi.org/10.1016/j.matpr.2018.04.150.
[26] V.K. Champagne, D.J. Helfritch, S.P.G. Dinavahi, P.F. Leyman, Theoretical and experimental particle velocity in cold spray, J. Therm. Spray Technol. 20 (2011) 425–431, https://doi.org/10.1007/s11666-010-9530-z.
[27] Sigma-Aldrich. https://www.sigmaaldrich.com/, 2021.
[28] J.M. Hoey, A. Lutfurakhmanov, D.L. Schulz, I.S. Akhatov, A review on aerosol-based direct-write and its applications for microelectronics, J. Nanotechnol. 2012 (2012), https://doi.org/10.1155/2012/324380.
[29] H. Ounis, G. Ahmadi, J.B. McLaughlin, Brownian diffusion of submicrometer particles in the viscous sublayer, J. Colloid Interface Sci. 143 (1991) 266–277, https://doi.org/10.1016/0021-9797(91)90458-K.
[30] W. Ranz, Evaporation from drops 1, Chem. Eng. Prog. 48 (1952) 173–180.
[31] W.E. Ranz, W.R. Marshall, Evaporation from drops: II, Chem. Eng. Prog. 48 (1952) 173–180.
[32] M.W. Lee, J.J. Park, D.Y. Kim, S.S. Yoon, H.Y. Kim, D.H. Kim, S.C. James, S. Chandra, T. Coyle, J.H. Ryu, W.H. Yoon, D.S. Park, Optimization of supersonic nozzle flow for titanium dioxide thin-film coating by aerosol deposition, J. Aerosol Sci. 42 (2011) 771–780, https://doi.org/10.1016/j.jaerosci.2011.07.006.
[33] J. Pattison, S. Celotto, A. Khan, W. O'Neill, Standoff distance and bow shock phenomena in the cold spray process, Surf. Coat. Technol. 202 (2008) 1443–1454, https://doi.org/10.1016/j.surfcoat.2007.06.065.
[34] A. Sova, S. Grigoriev, A. Kochetkova, I. Smurov, Influence of powder injection point position on efficiency of powder preheating in cold spray: numerical study, Surf. Coat. Technol. 242 (2014) 226–231, https://doi.org/10.1016/j.surfcoat.2013.10.078.
[35] C. Chen, B. Zhao, Some questions on dispersion of human exhaled droplets in ventilation room: answers from numerical investigation, Indoor Air 20 (2010) 95–111, https://doi.org/10.1111/j.1600-0668.2009.00626.x.

[36] L. Xu, X. Zhou, J. Li, Y. Hu, H. Qi, W. Wen, K. Du, Y. Ma, Y. Yu, Numerical simulations of molten breakup behaviors of a de Laval-type nozzle, and the effects of atomization parameters on particle size distribution, Processes. 8 (2020) 1027, https://doi.org/10.3390/pr8091027.

[37] A.H. Lefebvre, V.G. McDonell, Atomization and Sprays, 2017, https://doi.org/10.1201/9781315120911.

[38] S.H. Zahiri, W. Yang, M. Jahedi, Characterization of cold spray titanium supersonic jet, J. Therm. Spray Technol. 18 (2009) 110–117, https://doi.org/10.1007/s11666-008-9278-x.

[39] D.L. Gilmore, R.C. Dykhuizen, R.A. Neiser, T.J. Roemer, M.F. Smith, Particle velocity and deposition efficiency in the cold spray process, J. Therm. Spray Technol. 8 (1999) 576–582, https://doi.org/10.1361/105996399770350278.

[40] H. Ghassemi, S.W. Baek, Q.S. Khan, Experimental study on evaporation of kerosene droplets at elevated pressures and temperatures, Combust. Sci. Technol. 178 (2006) 1669–1684, https://doi.org/10.1080/00102200600582392.

[41] T. Kitano, J. Nishio, R. Kurose, S. Komori, Effects of ambient pressure, gas temperature and combustion reaction on droplet evaporation, Combust. Flame 161 (2014) 551–564, https://doi.org/10.1016/j.combustflame.2013.09.009.

[42] S.V. Klinkov, V.F. Kosarev, A.A. Sova, I. Smurov, Deposition of multicomponent coatings by cold spray, Surf. Coat. Technol. 202 (2008) 5858–5862, https://doi.org/10.1016/j.surfcoat.2008.06.171.

[43] M.V. Rukosuyev, O. Barannyk, P. Oshkai, M.B.G. Jun, Design and application of nanoparticle coating system with decoupled spray generation and deposition control, J. Coat. Technol. Res. 13 (2016) 769–779, https://doi.org/10.1007/s11998-016-9788-2.

[44] VixOneTM™ Nebulizers | Westmed, Inc., n.d. https://westmedinc.com/vixone/. (Accessed 26 January 2021).

[45] M. Marzbali, A. Dolatabadi, High-speed droplet impingement on dry and wetted substrates, Phys. Fluids 32 (2020) 112101, https://doi.org/10.1063/5.0020977.

[46] S. Nakade, M. Matsuda, S. Kambe, Y. Saito, T. Kitamura, T. Sakata, Y. Wada, H. Mori, S. Yanagida, Dependence of TiO_2 nanoparticle preparation methods and annealing temperature on the efficiency of dye-sensitized solar cells, J. Phys. Chem. B 106 (2002) 10004–10010, https://doi.org/10.1021/jp020051d.

[47] S. Ito, T. Takeuchi, T. Katayama, M. Sugiyama, M. Matsuda, T. Kitamura, Y. Wada, S. Yanagida, Conductive and transparent multilayer films for low-temperature-sintered mesoporous TiO_2 electrodes of dye-sensitized solar cells, Chem. Mater. 15 (2003) 2824–2828, https://doi.org/10.1021/cm021051t.

[48] S.Q. Fan, C.J. Li, G.J. Yang, L.Z. Zhang, J.C. Gao, Y.X. Xi, Fabrication of nano-TiO_2 coating for dye-sensitized solar cell by vacuum cold spraying at room temperature, J. Therm. Spray Technol. (2007) 893–897, https://doi.org/10.1007/s11666-007-9090-z. Springer.

[49] N.J. Wilkinson, M.A.A. Smith, R.W. Kay, R.A. Harris, A review of aerosol jet printing—a non-traditional hybrid process for micro-manufacturing, Int. J. Adv. Manuf. Technol. 105 (2019) 4599–4619, https://doi.org/10.1007/s00170-019-03438-2.

[50] S.Q. Fan, G.J. Yang, C.J. Li, G.J. Liu, C.X. Li, L.Z. Zhang, Characterization of microstructure of nano-TiO_2 coating deposited by vacuum cold spraying, Proc. Int. Therm. Spray Conf. (2006) 513–517, https://doi.org/10.1361/105996306X146901.